A&A 439, 413–425 (2005)
DOI: 10.1051/0004-6361:20042583

Astronomy & Astrophysics

The XMM-LSS survey

The XMDS/VVDS 4σ catalogue⋆,⋆⋆

L. Chiappetti[1], M. Tajer[2,5], G. Trinchieri[2], D. Maccagni[1], L. Maraschi[2], L. Paioro[1], M. Pierre[3], J. Surdej[4], O. Garcet[4], E. Gosset[4], O. Le Fèvre[6], E. Bertin[7], H. J. McCracken[7], Y. Mellier[7], S. Foucaud[1], M. Radovich[8], V. Ripepi[8], and M. Arnaboldi[9]

[1] INAF IASF, Sezione di Milano "G.Occhialini", via Bassini 15, 20133 Milano, Italy
e-mail: lucio@mi.iasf.cnr.it
[2] INAF Osservatorio di Brera, via Brera 28, 20121 Milano, Italy
[3] CEA/DSM/DAPNIA Service d'Astrophysique, Saclay, 91191 Gif-sur-Yvette, France
[4] Institut d'Astrophysique et de Géophysique, Université de Liège, Allée du 6 Août 17, 4000 Liège 1, Belgium
[5] Università degli Studi di Milano – Bicocca, Dipartimento di Fisica, Piazza della Scienza 3, 20126 Milano, Italy
[6] Laboratoire d'Astrophysique de Marseille, Traverse du Siphon, 13376 Marseille, France
[7] Institut d'Astrophysique de Paris, 89bis bvd Arago, 75014 Paris, France
[8] INAF Osservatorio di Capodimonte, via Moiariello 16, 80131 Napoli, Italy
[9] INAF Osservatorio Astronomico di Torino, via Osservatorio 20, 10025 Pino Torinese, Italy

Received 21 December 2004 / Accepted 26 April 2005

Abstract. We present a first catalogue of X-ray sources resulting from the central area of the XMM-LSS (Large Scale Structure survey). We describe the reduction procedures and the database tools we developed and used to derive a well defined catalogue of X-ray sources. The present catalogue is limited to a sub-sample of 286 sources detected at 4σ in the 1 deg^2 area covered by the photometric VVDS (VIRMOS VLT Deep Survey), which allows us to provide optical and radio identifications. We also discuss the X-ray properties of a larger X-ray sample of 536 sources detected at >4σ in the full 3 deg^2 area of the *XMM* Medium Deep Survey (XMDS) independently of the optical identification. We also derive the log N – log S relationship for a sample of more than one thousand sources that we discuss in the context of other surveys at similar fluxes.

Key words. X-ray: general – surveys – quasars: general – catalogs

1. Introduction

The XMDS (*XMM* Medium Deep Survey) is an X-ray survey based on the pooling of a significant fraction of the *XMM-Newton* guaranteed time of three "hardware institutes" (IASF Milano for XMM-EPIC, Liège for XMM-OM and CEA Saclay for XMM-SSC).

The XMDS pointings lie at the heart of the full, larger *XMM* Large Scale Structure (XMM-LSS) Survey (see Pierre et al. 2004), to which we refer for a discussion of the motivations and the choice of the sky field.

About two thirds of the XMDS area are covered in the optical band by the VVDS (VIRMOS VLT Deep Survey) both by *UBVRI* photometry (Le Fèvre et al. 2004) and by multi-object spectroscopy with VIMOS (Le Fèvre et al. 2005), by an associated radio survey at 1.4 GHz (Bondi et al. 2003) and by a GALEX Early Release Observation (Arnouts et al. 2005).

The XMM-LSS area has been covered by an associated radio survey at 74 and 325 MHz (Cohen et al. 2003) and will be covered by surveys in other bands like SWIRE (Lonsdale et al. 2003), the CFHTLS (see web site[1]) and by our own follow up observations (Pierre et al. 2004).

Thus, for these areas, multiwavelength information exists or will be gathered in the future, allowing investigations of large scale structures and source populations (clusters, galaxies and AGN) at medium redshifts.

For internal usage within the XMDS and XMM-LSS consortia, and in the future also for public access, a database has been designed, which is presented in this paper together with the first results obtained from the analysis of the XMDS data.

The layout of the paper is as follows. The database tool devised to store the results of the XMM-LSS and XMDS and

⋆ The full catalogue illustrated in Table 3 is only available in electronic form at the CDS via anonymous ftp to cdsarc.u-strasbg.fr (130.79.128.5) or via
http://cdsweb.u-strasbg.fr/cgi-bin/qcat?J/A+A/439/413

⋆⋆ Appendix A is only available in electronic form at http://www.edpsciences.org

[1] http://www.cfht.hawaii.edu/Science/CFHLS/

associated surveys is described in Sect. 2. Section 3 contains the analysis procedure (closely following that of Baldi et al. 2002) used to generate source lists from the 19 *XMM* pointings of the XMDS using a threshold that ensures a small number of spurious sources. Different selection criteria are then applied to obtain samples used for different purposes. A relatively low probability threshold is used to compute the $\log N - \log S$ relation presented and discussed in Sect. 4. The analysis of the X-ray characteristics is restricted to sources with a signal to noise ratio larger than 4, and the results are presented in Sect. 5. Only a fraction of the XMDS area is covered by the VVDS survey. For the latter area the identification procedure based on the photometric VVDS data and the derived optical vs. X-ray properties are described in Sect. 6.

Preliminary accounts of this work have been presented at recent conferences (Maraschi et al. 2003; Tajer et al. 2004).

2. The database and catalogue

2.1. The LSS database

The web site of the XMM-LSS Master Catalogue[2] has been designed as a front end to access the database containing the catalogues, both as a working tool for the XMDS and XMM-LSS consortia and, in the near future, for public access.

The query interface uses a Java servlet (communicating via JDBC protocol to the underlying MySQL[3] database) to manage the permissions of different groups of people to access different (parts of) database tables, to perform selections into multiple tables in an user-friendly way, to have a quick look at the data and to export results as ASCII or FITS files.

The database presently includes *database tables* for the results of the X-ray pipelines, VVDS photometry for objects within a 40″ box around an X-ray source, radio and other catalogues as reported in Sect. 6.1; it also provides links to *data products* like X-ray images and exposure maps, finding charts in the *I* band, radio maps, etc.

The database includes also pre-calculated correlation tables, which link the sequence identifiers of objects in an X-ray table with their neighbours in other tables according to predefined proximity criteria (e.g. a 40″ box or a 6″ radius), and greatly speed up queries which involve a couple of tables.

Correlations between more than two tables are managed similarly by multi-column correlation tables generated by our identification procedure described below in Sect. 6.1. They are also used to build *virtual tables*, i.e. simultaneous views of columns taken from different individual tables, or even of results of algebraic operations between different columns.

Usage of appropriate MySQL syntax during the composition of a query allows the production of results of arbitrary complexity as output from our database, like e.g. `ds9` region files, or the LaTeX code for the catalogue table reported here (Table 3).

2.2. The catalogue

In this paper we publish, as a first part of the XMDS catalogue, the results of the identification procedure described in Sect. 6.1, i.e. a catalogue of 286 X-ray sources detected at more than 4σ and located in the VVDS area. Further releases will also include sources already present in our database and detected at a lower S/N and/or located outside the VVDS area.

Our current choice allows us to present a catalogue inclusive of reliable (though not spectroscopically confirmed) identifications and of the basic optical and radio characteristics of the X-ray sources.

The catalogue published electronically at CDS along with the present paper includes a rather reduced, manageable number of columns. A printout sample of the catalogue in tabular form is presented in Table 3. Comments on individual sources are presented in Appendix A.

Since our database contains much more information than what is included in the published catalogue, we plan to open access to our database query engine, in accordance with the "legacy policy" of the XMM-LSS survey.

Usage of our database interface will allow the user to make selections on the datasets, to access additional columns (including e.g. X-ray fluxes in all bands, photometry in additional bands, radio fluxes, identification ranks and flags, technical information, etc.) which is not practical to include here, and to generate (and operate upon) expressions involving columns.

The query interface will be accessible from the time the paper is accepted at `http://cosmos.mi.iasf.cnr.it/~lssadmin/Website/LSS/Query` logging in as user `xmds`, password `guest` in workspace `public`.

3. Observations and data reduction

3.1. Observations

The XMDS observations consist of 19 overlapping pointings (typical duration in the range 20−25 ks), covering a contiguous area of about 3 deg^2. The sky location of the combined field of view (FOV) of the pointings is shown in Fig. 1.

The observations were performed by *XMM-Newton* (Jansen et al. 2001), with the EPIC MOS (Turner et al. 2001) and pn (Strüder et al. 2001) cameras, between July 2001 and January 2003. A basic journal of observations is reported in Table 1, containing the ESA dataset identifier that can be used to inquire for further details at the ESA *XMM* archive.

The XMDS fields are surrounded at present by 32 additional shorter (typically 10 ks) pointings (B01 to B32) performed in AO1 and AO2 as part of the XMM-LSS program. More detailed information is available on an ancillary page of the XMM-LSS Master Catalogue web site[4].

3.2. Generation of the X-ray source list

The reduction of the XMDS data has been performed in Milan using a streamlined version of the pipeline developed by

[2] `http://cosmos.mi.iasf.cnr.it/~lssadmin/Website/LSS`

[3] MySQL is an open source database server developed by MySQL AB (see `http://www.mysql.com`).

[4] `http://cosmos.mi.iasf.cnr.it/~lssadmin/Website/LSS/Anc/goepic.html`

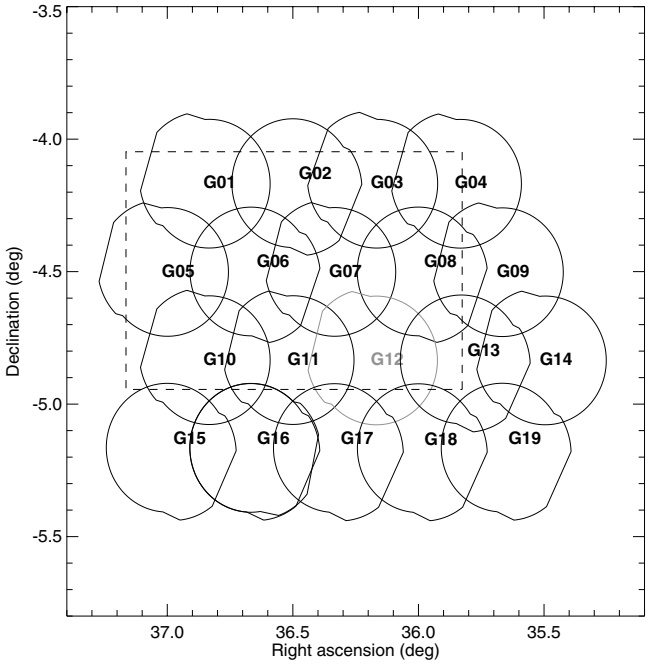

Fig. 1. Location of the XMDS pointings on the sky: the approximate FOV footprint (with the pn protruding at the actual roll angle) is shown (solid lines); the gray colour for field G12 indicates that it has not been used (see text). The dashed rectangle indicates the area of VVDS photometry.

Baldi et al. (2002) for the HELLAS2XMM survey. We refer to the latter paper for the formalism and procedure, and only mention here the main points and the few differences.

We used the *XMM-Newton* Science Analysis System (XMM-SAS) v5.4.1, whose tasks `emproc` and `epproc` now provide a reliable identification of the location of bad pixels. To remove data contaminated by soft proton flares, we used *fixed* thresholds (on the global background above 10 keV) of 0.15 counts s^{-1} for MOS and 0.35 counts s^{-1} for pn: as a result of this choice, field G12 could not be analysed because the background was almost constantly above these thresholds. A mosaic of our X-ray images is shown in Fig. 2.

As in Baldi et al. (2002), we ran the source detection (inclusive of background computation) and characterization procedure on merged MOS and pn data in *five* different energy bands, which we designate as: A (0.3−0.5 keV), B (0.5−2 keV), C (2−4.5 keV), D (4.5−10 keV) and CD (2−10 keV). We note that sources detected in the CD band do not result from the simple sum of detections in the separate C and D bands, but from the detection algorithm run on the full 2−10 keV band, while quantities referring to the total band ABCD (0.3−10 keV) are obtained by summation of the results in the individual bands.

We have used the XMM-SAS tasks `eboxdetect` and `emldetect` to obtain a list of candidate source positions, but net counts and associated parameters are obtained from our own program written according to Baldi et al. (2002). In particular fluxes were computed for a power law spectrum with $\Gamma = 1.7$ and $N_{\rm H} = 2.61 \times 10^{20}$ cm^{-2} (i.e. the average galactic column density in the XMDS field direction (Dickey & Lockman 1990)), using conversion factors calculated from response matrices generated consistently with the event selections used in our pipeline. In particular, as in Baldi et al. (2002), we used a conservative pattern selection of single and double events for MOS, and only single events for pn. Since the count rates are derived in regions including a fixed percentage (68%) of the expected flux from a point source (whose radius depends on off-axis positions), our fluxes are correct for point-sources. The fact that a source may fall close to (or on) an inter-CCD gap is taken into account in flux computation by proper usage of the EPIC calibration files, and by the usage of exposure maps in the measurement of the count rate. This should be an acceptable approximation (the same used by Baldi et al. 2002). Anyhow, we record in our database a flag indicating whether a source is close to a FOV edge or to CCD borders or gaps.

For insertion in our database, we retain only sources that have a chance detection probability less than 2×10^{-4} *in at least one energy band*. In the 19 useful pointings of the survey, we detected 1322 X-ray sources (including multiple detections in overlapping regions, see Table 2), satisfying the probability threshold $P < 2 \times 10^{-4}$. In this work we present subsets chosen with more stringent criteria: (1) all sources detected with chance probability less than 2×10^{-5} to derive the $\log N - \log S$ relationship (Sect. 4); (2) X-ray sources detected with a signal to noise ratio larger than 4 in any one of the energy bands defined above (where the error σ_S on the net number of counts is calculated using the Poissonian approximation from the gross number of counts $\mathrm{cts_{img}}$

$$\sigma_{\rm S} = 1 + \sqrt{\mathrm{cts_{img}} + 0.75}$$

according to Gehrels 1986, as in Baldi et al. 2002) to study the mean X-ray properties of the brighter end of the sample (the 4σ sample, Sect. 5); (3) all sources in the 4σ sample covered by VVDS photometry, for which we present the catalogue (Sect. 2.2) and we discuss the X-ray/optical properties (Sect. 6).

The numbers of sources in each sample are reported in Table 2.

Note that in the present version we have analysed each pointing independently, in spite of the fact that the FOVs of adjacent pointings overlap. The same object could therefore be detected in more than one field. This fact is recognized only a posteriori (see Sect. 5). In what follows we will always specify whether the sample we consider includes multiple detections of the same source.

An independent pipeline is being developed in Saclay for the analysis of the entire XMM-LSS, using a wavelet technique and therefore best suited for extended sources (Pacaud et al. 2005, see a preliminary account in Pierre et al. 2004) and will be used as a basis for the future complete XMM-LSS catalogue.

4. The log *N* – log *S* relationship

We computed the $\log N - \log S$ distributions in the 0.5−2 and 2−10 keV bands as follows.

We have considered all sources with a detection probability in the 0.5−2 and 2−10 keV bands below $P = 2 \times 10^{-5}$. This is well below our acceptance threshold of 2×10^{-4}, ensuring

Table 1. Journal of XMDS observations[e].

Field	ESA obs id	Date	Pointing RA	Dec	Max exposure[c] (ks)	Shift[d] ΔRA (″)	ΔDec (″)
G01	011268 0101	28 Jan. 2002	02:27:25.4	–04:11:06.4	24.9	–1.60	0.00
G02	011268 0201	14 Jul. 2002	02:25:54.2	–04:09:05.6	9.8	0.00	–0.53
G03	011268 0301	19 Jan. 2003	02:24:45.6	–04:11:00.8	21.8	–0.53	1.07
G04	010952 0101	29 Jan. 2002	02:23:25.3	–04:11:07.6	25.8	–1.60	0.00
G05	011268 0401	02 Feb. 2002	02:28:05.1	–04:31:08.1	23.7	0.00	0.00
G06	011268 1301	26 Jul. 2002	02:26:34.4	–04:29:00.8	13.0	0.00	0.53
G07	011268 1001	30 Jan. 2002	02:25:25.3	–04:31:07.1	23.5	–0.53	–0.53
G08	011268 0501	25 Jul. 2002	02:23:54.6	–04:29:00.1	18.3	0.00	0.00
G09	010952 0601	31 Jan. 2002	02:22:45.2	–04:31:11.1	22.4	n/a	n/a
G10	010952 0201	29 Jan. 2002	02:27:25.4	–04:51:04.4	24.8	–0.54	0.53
G11	010952 0301	02 Feb. 2002	02:26:05.1	–04:51:06.1	21.9	0.00	0.53
G12[a]	010952 0401	01 Feb. 2002	02:24:45.4	–04:51:11.2	n/a	n/a	n/a
G13	010952 0501	03 Jul. 2001	02:23:13.1	–04:49:03.1	23.9	–2.67	–2.13
G14	011268 0801	31 Jan. 2002	02:22:04.1	–04:51:09.7	13.6	n/a	n/a
G15	011111 0101	06 Jul. 2001	02:27:54.1	–05:09:02.3	21.2	n/a	n/a
G16[b]	011111 0201	06 Jul. 2001	02:26:34.2	–05:09:03.1	3.9	n/a	n/a
G16[b]	011111 0701	14 Aug. 2001	02:26:35.2	–05:08:46.6	11.7	n/a	n/a
G17	011111 0301	03 Jul. 2001	02:25:14.3	–05:09:08.4	22.5	n/a	n/a
G18	011111 0401	03 Jul. 2001	02:23:54.1	–05:09:09.7	28.1	n/a	n/a
G19	011111 0501	04 Jul. 2001	02:22:34.0	–05:09:02.1	23.7	n/a	n/a

[a] Pointing G12 has not been used because of the high background level (see text).
[b] Pointing G16 has been repeated since the first instance was curtailed.
[c] The reported max exposure is the highest value in the exposure maps of the individual cameras, i.e. net of soft proton flares.
[d] The RA and DEC shifts are the astrometric correction applied (see text) for the fields which overlap the VVDS area and for which optical identification has been performed.
[e] More details available through our ancillary web page
`http://cosmos.mi.iasf.cnr.it/~lssadmin/Website/LSS/Anc/xmdsepic.html`

very few spurious sources in the sample while giving us a large dataset to compute the $\log N - \log S$.

We have generated a flux limit map for each X-ray field and energy band, which contains the faintest flux at which a source can be detected at the assumed level of significance above the local background. From these we have computed the sky coverage plotted in Fig. 3. This considers all fields as independent areas, consistently with our detection procedure (see Sect. 3.2), so the full sky coverage is the sum of all areas surveyed.

Our faintest flux is $\sim 10^{-15}$ erg cm^{-2} s^{-1} in the 0.5−2 keV band and $\sim 7 \times 10^{-15}$ erg cm^{-2} s^{-1} in the 2−10 keV band.

In Fig. 4 we plot the cumulative $\log N - \log S$ in the 0.5−2 keV band (upper left panel, 1028 sources) and in the 2−10 keV band (lower left panel, 328 sources). The plots relative to individual fields have also been produced and inspected and do not show significant deviations from the combined distribution.

The shapes of the (cumulative) $\log N - \log S$ are clearly curved and cannot be represented by a single power law. A fit to the cumulative distribution does not allow a meaningful computation of confidence limits on the parameters, because points and errors are not independent (Murdoch et al. 1973; Crawford et al. 1970). Therefore we computed the differential $\log N - \log S$ by binning (in logarithmic space) the number $N(F)$ of sources with flux F into flux bins of width ΔF_i (i.e. between fluxes $F_{j\min}$ and $F_{j\max}$), then computing the average sky coverage A_i in the bin. The ith bin of the differential curve $n(F)$ (shown in the right panels of Fig. 4) is given by

$$n(F)_i = \sum_{F_{j\min}}^{F_{j\max}} \frac{N(F_j)}{\Delta F_i A_i}.$$

A statistical error due to the Poissonian error on the number of sources is assigned to each bin. Again, we confirm that a single power law does not give a good fit. Therefore we used a broken power law.

For the 0.5−2 keV band, the best fit is

$$n(F) = \begin{array}{ll} 6.515 \times 10^3 \times F_{15}^{-2.62} & F_{15} > 10.58 \\ 384.2 \times F_{15}^{-1.42} & F_{15} < 10.58. \end{array}$$

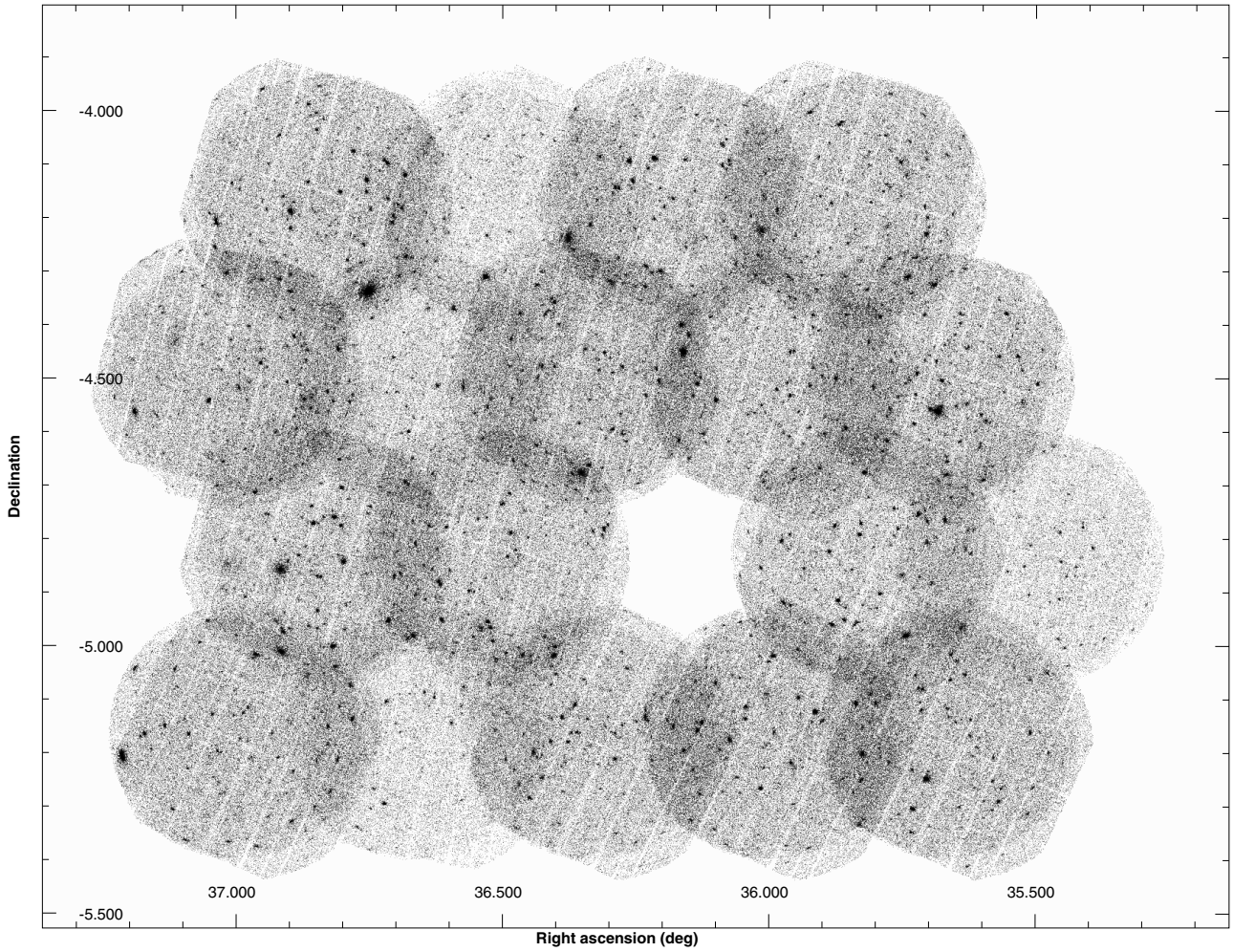

Fig. 2. Mosaic of our X-ray images in the total (0.3−10 keV) band. No exposure map correction has been applied to this figure.

Table 2. Total number of sources and sources detected in the *B* and *CD* bands respectively for the samples presented in the paper. For the $P < 2\times10^{-4}$, $P < 2\times10^{-5}$ and the first line of the 4σ sample, numbers refer to detections (i.e. include multiple detections of the same source in different fields), while for the second line of the 4σ sample and for the 4σ VVDS sample numbers refer to *independent* sources.

Sample	$N_{\rm tot}$	N_B	N_{CD}
$P < 2\times10^{-4}$	1322	1166	419
$P < 2\times10^{-5}$	1129	1028	328
4σ (detections)	612	591	158
4σ (independent)	536	518	143
4σ VVDS	286	278	73

All fluxes F_{15} are normalized to 10^{-15} erg cm^{-2} s^{-1}. 90% confidence limits on slopes are $2.62^{+0.25}_{-0.22}$ and $1.42^{+0.14}_{-0.15}$, while the break position is in the range $1.06^{+0.30}_{-0.22}\times10^{-14}$ erg cm^{-2} s^{-1}.

For the 2−10 keV band we find

$$n(F) = 4.483\times10^{4}\times F_{15}^{-2.91}$$

for $F_{15} > 21.4$, with 90% errors on slope $2.91^{+0.45}_{-0.30}$ and break at $2.14^{+0.81}_{-0.54}\times10^{-14}$ erg cm^{-2} s^{-1}. At lower fluxes the slope is not well constrained: the best fit is 1.53, but the confidence interval ranges between 0.37 and 2.04.

In Fig. 4 we show the fit results both in the differential and the cumulative forms for a better comparison with the literature that gives sometimes cumulative (e.g. Baldi et al. 2002; Moretti et al. 2003), sometimes differential plots (e.g. Yang et al. 2004; Harrison et al. 2003). Given the uncertainties in the fits, we prefer the comparison with the actual data where possible.

Our probability threshold $P < 2\times10^{-5}$ is one of those used in Baldi et al. (2002). Since our procedure is very similar to theirs and the flux range is nearly the same, the $\log N - \log S$ should in principle be almost identical. We find consistency (within errors) with the integral HELLAS2XMM distributions for the lower fluxes: $F_{0.5-2} \lesssim 3\times10^{-14}$ erg cm^{-2} s^{-1} and $F_{2-10} \lesssim 2\times10^{-14}$ erg cm^{-2} s^{-1}, while at higher fluxes we are nominally lower, but, taking into account the purely statistical error on the number of sources, we are consistent with the lower envelope of the Baldi et al. (2002) relationship.

A good agreement is also found with the *Chandra* Large Synoptic X-ray Survey (CLASXS, Yang et al. 2004) and with the Serendipitous Extragalactic X-ray Source Identification (SEXSI, Harrison et al. 2003) program, in the common flux range. We compared the differential plots and found

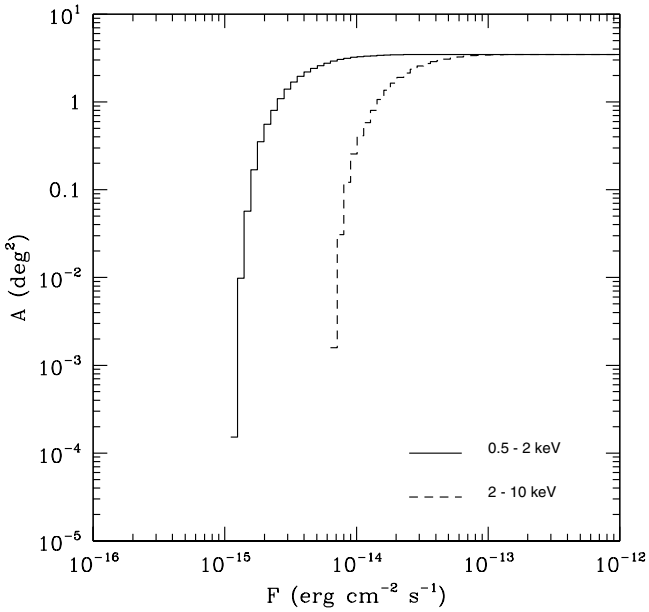

Fig. 3. Sky coverage for sources detected at $P < 2\times10^{-5}$ in the *B* band (solid line) and in the *CD* band (dashed line) computed considering all fields as independent (see text).

consistency with the CLASXS survey in the soft band (no plot in that band is given in Harrison et al. 2003). In the hard band we are consistent with the SEXSI survey, but we are systematically lower than the CLASXS points; this is not surprising, given that Yang et al. (2004) find that their total counts at $F_{2-8} \sim 10^{-14}$ erg cm^{-2} s^{-1} are ∼70% higher than those of Moretti et al. (2003), who use Baldi et al. (2002) data for the flux range we are interested in.

The sky location of the XMDS survey has been intentionally chosen in order to avoid known bright X-ray sources and this could therefore explain, at least partially, the low density observed in our survey for fluxes above a few 10^{-14} erg cm^{-2} s^{-1}. On the other hand, Yang et al. (2004) interpret their overdensity as an indication of an underlying large scale structure. We note that the CLASXS, like the XMDS, is constructed on contiguous pointings, while the HELLAS2XMM and the SEXSI surveys are serendipitous surveys: it seems reasonable that the number count difference we find between the different surveys is caused by cosmic variance.

5. X-ray properties of the *total XMDS* 4σ sample

One of our criteria for the definition of a sample is the presence of a localized X-ray count excess with signal to noise ratio (as defined in Sect. 3.2) ≥4 in at least one of the energy bands (the "4σ sample"). This results in 612 *detections*. Taking into account multiple detections (same source detected in different overlapping fields) the total number of *independent sources* reduces to 536. All detections in different pointings with X-ray positions closer than 6″ have been automatically considered as multiple detections of the same source. For larger separations (up to 18″, which can be considered as a boundary for suspicious overlaps, since there are only 2 pairs of sources detected in the *same* field which are closer than such a distance, one at 8.7″and one at 15.9″), we examined each of the 8 pairs and recovered 2 cases: one is included in our catalogue and is discussed in Appendix A, the other has a distance of 6.4″, but one detection is outside the FOV of one camera. For all multiple detections we used the position and derived parameters from the detection that gave the highest significance, unless the source falls outside the FOV of one camera, or close to an inter-CCD gap. We do not detect any significant flux variation in the multiply detected sources with the possible exception of three, which are however close to inter-CCD gaps. The apparent flux decrease in the 0.5−2 keV band from the brightest observation in each couple would be of –35%, –65% and –28%, with a significance of ∼3.5, 3.9 and 4.5σ respectively.

5.1. Fluxes and hardness ratios

The flux distribution of the sources in the 4σ sample is shown in Fig. 5 for sources detected in the energy bands 0.5−2 (left panel) and 2−10 keV (right panel) respectively.

We find that 518 sources (∼97%) are included in the sample because of their detection in the 0.5−2 keV (*B*) band, while only 143 (∼27%) satisfy the detection criterion in the 2−10 keV (*CD*) band. Clearly most of the latter are *also* detected in the *B* band. We do not have any source included in the sample because of its detection in the 4.5−10 keV band *only*, and only 16 hard sources (∼10%) are not detected in the 0.5−2 keV band. As indicated by Fig. 5, we find a posteriori $F_X \sim 2.5\times10^{-15}$ erg cm^{-2} s^{-1} as the flux limit in the *B* band and $F_X \sim 2\times10^{-14}$ erg cm^{-2} s^{-1} in the *CD* band.

A spectral analysis of the brighter sources is in progress. Here we present the results of the hardness ratio analysis that can be done for a significantly larger number of sources, and is the only spectral analysis possible for the fainter sources in the sample.

To this end we note that, even if a source does not satisfy the detection threshold in a band different from the one that motivated the inclusion in the sample, we have an estimate of the counts and fluxes in all bands considered, which we can use to get spectral information. Let us define:

$$\mathrm{HR} = \frac{CR_{2-10} - CR_{0.5-2}}{CR_{2-10} + CR_{0.5-2}}$$

$$\mathrm{HR_{cb}} = \frac{CR_{2-4.5} - CR_{0.5-2}}{CR_{2-4.5} + CR_{0.5-2}}$$

$$\mathrm{HR_{dc}} = \frac{CR_{4.5-10} - CR_{2-4.5}}{CR_{4.5-10} + CR_{2-4.5}}$$

where *CR* are the net count rates in the given energy band corrected for PSF and vignetting. We only include sources for which we have a reasonable estimate of the flux (i.e. a signal-to-noise ratio ≥2) in the 4.5−10 keV band: upper limits in such a band do not carry significant information since they provide only an upper limit to $\mathrm{HR_{dc}}$, which is expected for fainter sources with the canonical unabsorbed power law spectrum. On the contrary upper limits from the 0.5−2 keV band are interesting as they provide lower limits to $\mathrm{HR_{cb}}$.

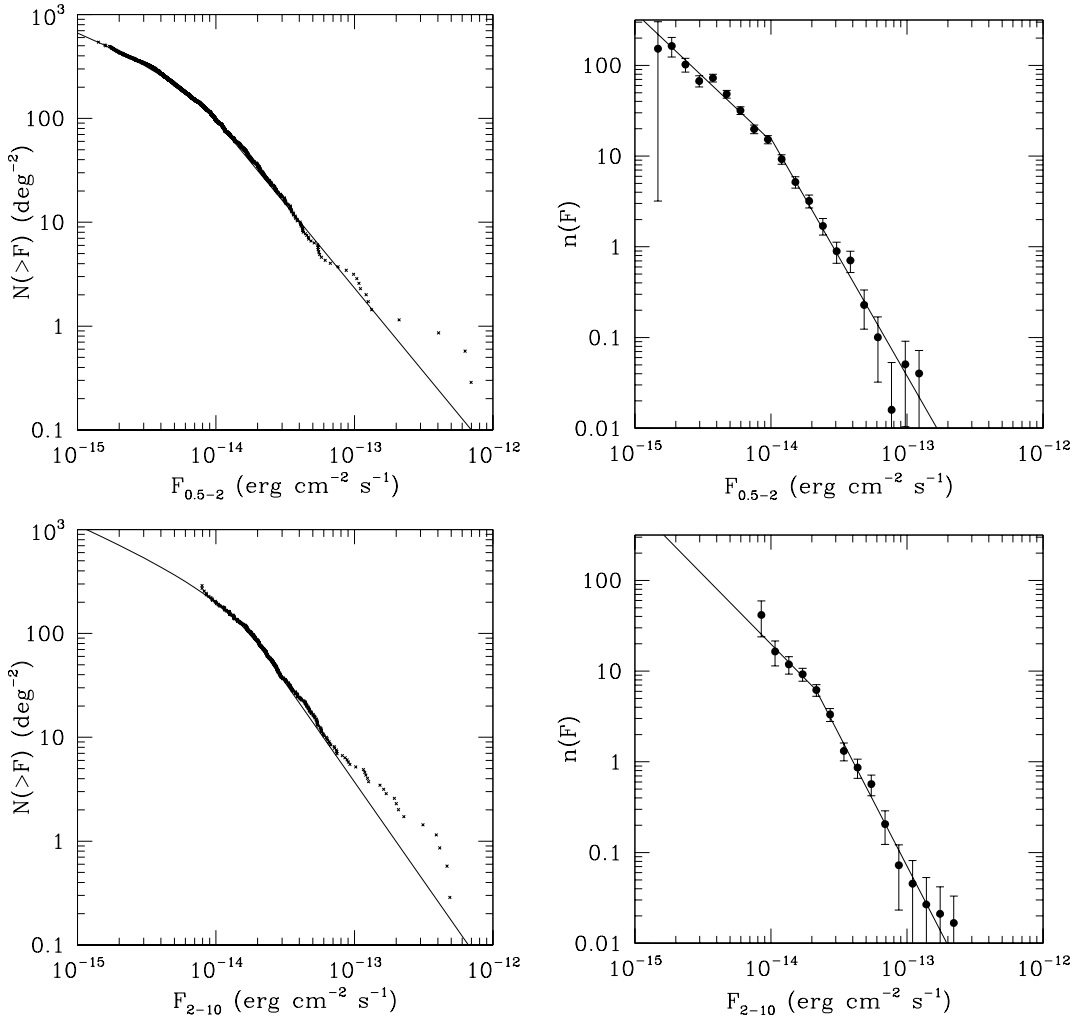

Fig. 4. Log N − log S of sources detected at $P < 2 \times 10^{-5}$ in band B in the cumulative (*upper left panel*) and differential (*upper right panel*) form and the same in band CD (*lower left and right panels*). The units of $n(F)$ are number per 10^{-15} erg cm^{-2} s^{-1} and deg^{-2}. Our best fits are reported as solid lines on the differential plots and have also been converted to the cumulative form.

We verified that the values obtained from the combined count rates from different cameras are consistent with those computed from single camera data.

In Fig. 6 we plot the main hardness ratio HR as a function of the 2−10 keV flux. Also shown in the figure are dashed lines indicating the hardness ratios expected for a simple power law model with spectral index $\Gamma = 1.7$ and increasing values of the absorbing column $N_{\rm H}$. This plot shows that ∼30% of sources detected in the CD band have hardness ratios consistent with $N_{\rm H} > 10^{21.5}$ cm^{-2}, for $z = 0$. Note that if sources are at higher redshifts, the horizontal lines for different values of $N_{\rm H}$ shift downwards, i.e. the same hardness ratio corresponds to a higher absorption column.

Within our current sample, we do not find a spectral hardening with decreasing X-ray flux as reported by other authors; however our statistics in the hard band is lower than those from other surveys. On the other hand, it appears from numbers in Table 2 that the fraction of sources in the hard band increases when the sample is larger (from 26% in the 4σ sample to 32% in the total $P < 2 \times 10^{-4}$ sample). Since a less restrictive threshold implies a lower flux limit, we can infer that the fraction of hard sources should increase as the flux decreases.

Figure 7 shows the so-called X-ray colour-colour diagram, i.e. the plot of the hardness ratio between the harder bands $\mathrm{HR_{dc}}$ vs. the hardness ratio between soft and hard bands $\mathrm{HR_{cb}}$.

Sources with HR consistent with $N_{\rm H} > 10^{22}$ cm^{-2} in Fig. 6 occupy the same locus in Fig. 7 (or $N_{\rm H} > 10^{23}$ cm^{-2} if we consider that sources are at $z \sim 1$). This singles them out as promising candidates for more detailed studies.

In spite of the relatively small number of objects, it is worth noting that a few sources with low values of $\mathrm{HR_{cb}}$ and high values of $\mathrm{HR_{dc}}$ are present: these are not consistent with a simple power law model. In particular, their location in the diagram at $\mathrm{HR_{dc}} > -0.2$ and $\mathrm{HR_{cb}} < -0.5$ could suggest a concave spectral shape, due to the relative lack of signal around 2 keV. Such a shape could result from the superposition of an unabsorbed component on a flat/absorbed power law as often observed in obscured AGNs, where the unabsorbed component can be due to scattered or transmitted AGN continuum or to thermal and non thermal emission associated with starburst regions.

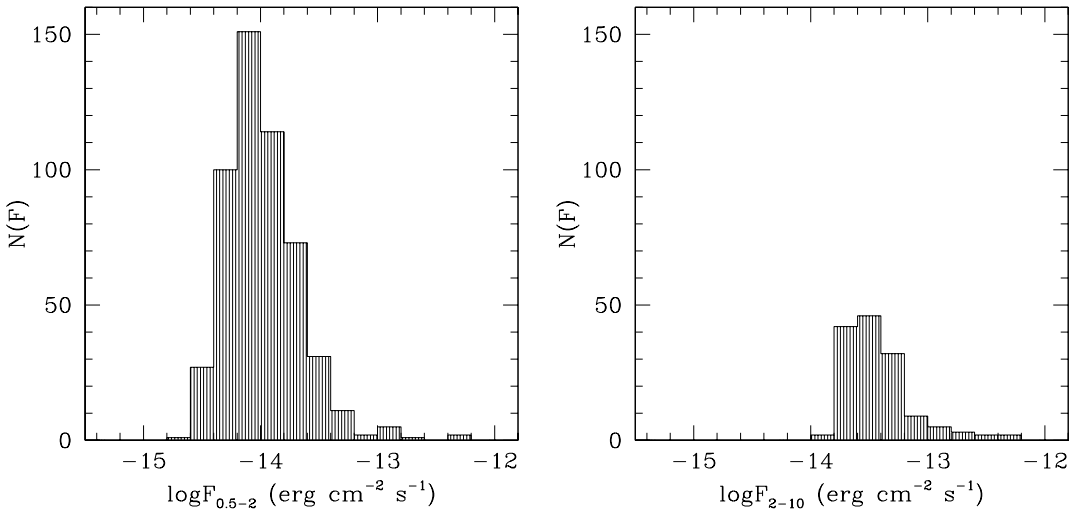

Fig. 5. Flux distribution in band *B* (*left panel*) and in band CD (*right panel*) for the total 4σ sample. The hatched area gives the distribution of the sources detected at $\geq 4\sigma$ *in the concerned band.*

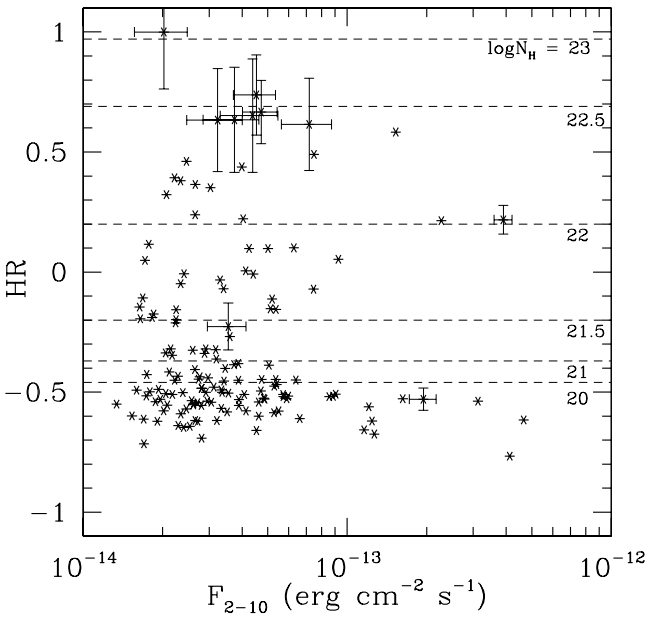

Fig. 6. Hardness ratio HR vs. 2−10 keV flux for all sources detected at $\geq 4\sigma$ in the CD band (asterisks). Only a few typical error bars are shown to avoid figure overcrowding, inclusive of all those detected at $\leq 2\sigma$ in the *B* band. Dashed lines indicate hardness ratios expected for an absorbed power law spectrum with energy index $\Gamma = 1.7$ and intrinsic N_H as reported in the label.

6. The XMDS/VVDS 4σ sample

6.1. The identification procedure

For the generation of our sample of candidate identified X-ray sources we have used the following data sources (database tables and data products).

- The database table of X-ray sources from our pipeline.
- The optical tables with the VVDS *UBVRI(JK)* photometry including both sources with reliable photometric data and objects whose photometry is flagged as unreliable because the objects are saturated, masked or close to the borders of the VVDS area. In addition, we have used the associated finding charts. Data quality and limiting magnitudes are discussed in McCracken et al. (2003) and Radovich et al. (2004).
- The table with the VIRMOS 1.4 GHz radio catalogue (Bondi et al. 2003) which covers the 1 deg^2 VVDS area at a depth of 80 μJy and a resolution of 6″.
- The table with the XMM-LSS radio catalogue (Cohen et al. 2003), a shallow survey at 74 (4 mJy, 5.6 deg^2) and 325 MHz (275 mJy, 110 deg^2) over a larger area encompassing the XMM-LSS fields. Occasionally we used the associated radio maps.
- The table with the tentative cluster candidates.
- The NED and SIMBAD database tables, containing pointers to objects within 20″ from an X-ray source. It should be noted that the VIRMOS 1.4 GHz catalogue has recently been inserted also in SIMBAD, which could result in a redundant association.

The identification process has followed a multi-step procedure, that also involved the determination of reliable X-ray/optical angular separation criteria for identifications and the testing of more automated identification procedures for future works.

First of all, we used our database to create the sample of X-ray sources that are within the VVDS area (i.e. for which we can provide a FITS finding chart, covering a 40″ box around the X-ray position, that we visually inspected).

For each unique X-ray source we have then conservatively considered all optical objects within a radius of 6″ from the X-ray position (see e.g. Waskett et al. 2004). This radius is considerably larger than the nominal SAS (`emldetect`) position error combined with the 2″ *XMM* astrometrical uncertainty. For such objects we have positions, magnitudes and a crude optical classification (star-like vs. extended) from the VVDS database.

We have identified the optical counterparts according to the following criteria: a) unique optical counterpart (67 objects); b) closest and brightest (Δmag > 2) counterpart (166 objects);

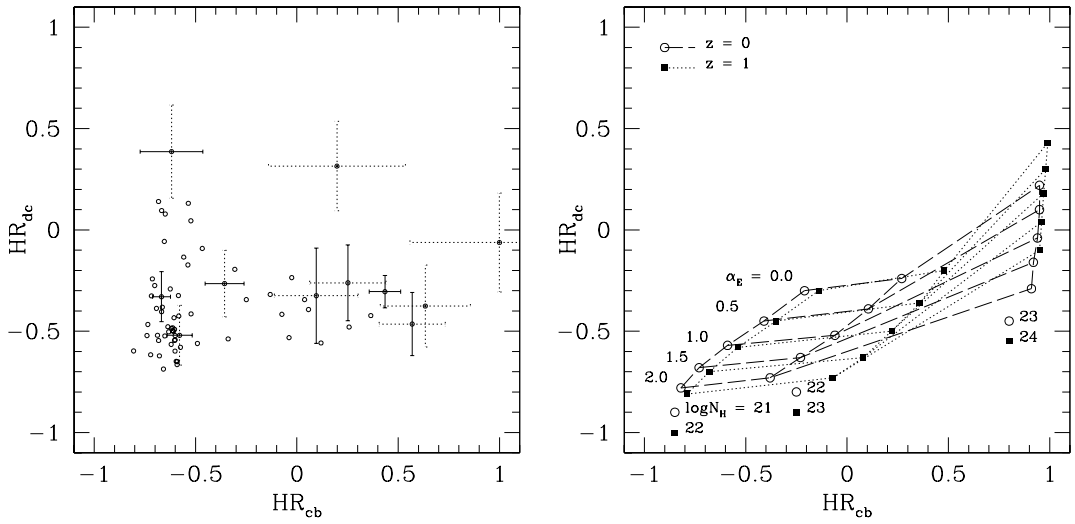

Fig. 7. Hardness ratio HR_{dc} vs. HR_{cb} for sources in the $\geq 4\sigma$ sample (*left panel*), which are also above 2σ in band *D*. Typical error bars are shown (dashed when the significance in the involved bands is below 4σ). Grids in right panel represent hardness ratios expected with a simple power law model for values of spectral index and N_H reported in the labels at $z = 0$ (empty circles and dashed lines) and at $z = 1$ (full squares and dotted lines).

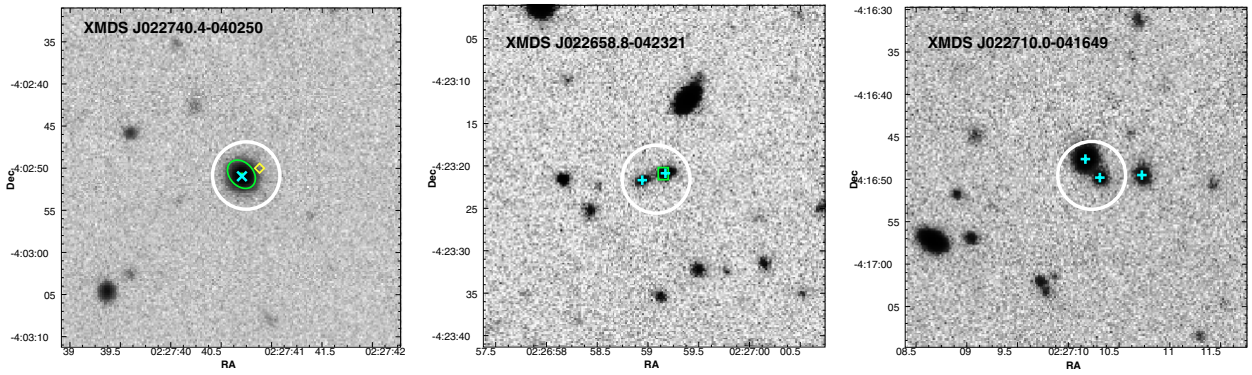

Fig. 8. Examples from our identification procedure: some representative *I* band finding charts (size $40'' \times 40''$) with overlays of the X-ray error circles (white thick at $4''$ radius), the positions of all optical sources within $6''$ (cyan X's and crosses respectively for point-like and possibly extended objects), the positions of NED catalogue objects (yellow diamonds) and the radio source error box (green rectangles) or extent (green ellipses). The printed figure is in grayscale: see the online edition for a colour version. Three cases are shown: an unique counterpart, an identification preferring a radio source, an ambiguous identification.

c) no optical counterpart down to $I \sim 25$, the magnitude limit of McCracken et al. (2003) (5 objects, of which 3 with no counterpart at all, 2 with a radio counterpart). We also used the presence of a radio counterpart as a preference criterion. The remaining cases [55] do not allow us to assign an unambiguous optical counterpart until spectroscopic confirmation of the source is available, so all possible optical counterparts are retained. 22 cases were flagged as suspect groups, clusters or simply crowded fields, of which half have however a dominant, unique counterpart. Examples of finding charts used in our identification procedure are shown in Fig. 8.

After a first pass with this procedure, we found evidence in some X-ray fields of a systematic rigid shift between the position of the X-ray sources and their counterparts (as high as $3''$ in field G13). We profitably used the pairs identified at such stage to compute (via the SAS task `eposcorr`) a rigid shift correction (see Table 1), and inserted in the database two additional columns with corrected X-ray positions. No rotational correction was required. See also Sect. 6.2 and Fig. 9. After this astrometric correction we repeated our inspection and ranking procedure.

This time-consuming identification process involved a number of iterations and intermediate steps, which we have recorded in the database with different flags and fields (that could identify for example the presence of a visually crowded field, the cross-correlation with a detection of the same source in a different field, the source and quality of the optical photometry). These will remain as part of the record for each source for future automatic database queries, but are not included in the catalogue attached to this paper.

The final identifications are reported in the catalogue presented here and have associated numerical codes that describe the quality (rank) of the identification, as described in point M of Table 3.

As a final step, we have computed the probability of chance coincidence between the X-ray source and the optical

Table 3. Sample of our X-ray catalogue. We report here only the first few lines of the catalogue to show the layout. The full catalogue will be available at CDS or through our database as described in Sect. 2.2. Comments on peculiar sources are reported in Appendix A.

A	B	C	D	E	F	G	H	I	J	K	L	M	N	O	P	Q	R	S	T	U	V	W
580	XMDS J022315.4-042558	02 23 15.5	-04 25 58.4	56.7	11.8	22.1	10.5	10.0	20.3	B	1	1	1.4				1				APMUKS(BJ) B022044.68-043934.9	580
839	XMDS J022315.3-044320	02 23 15.5	-04 43 18.4	48.2	10.8	22.3	9.8	3.9	9.0	B	0	2	2.1	25.45	0.16	24.24	0.36	1				839
310	XMDS J022316.3-042007	02 23 16.4	-04 20 07.8	121.8	15.7	1.0	7.2	12.2	0.5	B	0	0	1.8				1				BD-04 388	310
846	XMDS J022317.2-044035	02 23 17.4	-04 40 33.5	167.2	18.0	72.4	13.3	17.0	37.3	B	0	1	1.1	18.47	0.00	18.23	0.00	1				846
828	XMDS J022318.8-044616	02 23 19.0	-04 46 13.9	166.7	17.9	53.0	11.5	11.0	17.4	B	0	0	0.2	21.16	0.01	20.77	0.01	0				828
321	XMDS J022319.2-041648	02 23 19.4	-04 16 48.4	55.8	11.4	9.6	8.4	4.1	3.6	B	0	1	1.1	22.62	0.04	21.73	0.03	0				321
820	XMDS J022319.4-044732	02 23 19.6	-04 47 30.4	280.6	22.5	125.6	16.0	17.4	38.7	B	0	0	0.7	19.14	0.01	18.49	0.00	0				820
779	XMDS J022321.8-045740	02 23 22.0	-04 57 38.4	20.1	9.1	98.7	14.7	1.9	47.2	CD	0	0	1.0	20.35	0.01	19.47	0.01	1				779
333	XMDS J022324.9-041452	02 23 25.1	-04 14 52.2	70.5	12.9	28.5	9.8	4.7	9.4	B	0	1	0.6	21.83	0.02	21.31	0.02	0				333
550	XMDS J022326.0-043537	02 23 26.0	-04 35 37.1	115.3	15.3	31.3	10.6	17.7	25.1	B	1	1	1.0	23.16	0.04	22.33	0.04	0				550
315	XMDS J022326.3-041838	02 23 26.5	-04 18 38.5	51.6	11.5	8.9	8.4	4.6	4.0	B	0	0	0.5	24.29	0.08	23.27	0.07	0				315
782	XMDS J022326.3-045708	02 23 26.5	-04 57 05.1	122.8	15.8	62.2	12.3	11.4	29.1	B	0	0	1.5	20.74	0.01	20.49	0.01	1				782
789	XMDS J022329.1-045452	02 23 29.3	-04 54 50.8	245.2	21.2	52.0	11.5	22.0	24.0	B	2	1	1.2	20.25	0.01	19.92	0.01	0				789
789												2	3.5	22.13	0.02	21.45	0.02	0				789
571	XMDS J022330.2-043004	02 23 30.3	-04 30 04.2	121.7	15.7	47.0	11.7	14.0	27.6	B	1	0	1.7	20.18	0.01	19.94	0.01	0				571
825	XMDS J022330.6-044633	02 23 30.8	-04 46 31.8	303.2	23.3	100.4	14.8	20.5	33.6	B	0	1	0.8	24.44	0.12	23.37	0.08	0				825
840	XMDS J022330.9-044235	02 23 31.1	-04 42 33.0	59.1	12.4	37.6	10.6	6.3	20.8	B	2	2	5.4	24.77	0.14	24.59	0.24	0				840
780	XMDS J022332.0-045740	02 23 32.2	-04 57 38.7	184.5	18.7	49.5	11.6	18.1	24.6	B	0	0	0.7	19.99	0.01	19.63	0.01	1				780
354	XMDS J022332.2-041022	02 23 32.3	-04 10 22.1	128.4	16.2	9.3	7.6	7.7	2.8	B	0	0	0.3	17.77	0.00	16.93	0.00	2				354
807	XMDS J022333.0-044924	02 23 33.2	-04 49 22.5	143.8	16.7	48.0	11.3	11.2	17.9	B	2	1	0.9	20.60	0.01	20.26	0.01	0				807

A Internal sequence identifier.

B IAU catalogue name of the object (built from uncorrected coordinates as provided by the XMM-SAS); the X-ray properties of a source, i.e. columns from B to L, appear once only on the first catalogue entry for such a source. If the X-ray source has further possible counterparts, these columns are blank and their value is the same as the first entry with same sequence identifier.

C Astrometrically corrected RA (J2000).

D Astrometrically corrected Declination (J2000).

E Number of net counts in band *B*.

F Error on net counts in band *B*.

G Number of net counts in band *CD*.

H Error on net counts in band *CD*.

I Flux in 10^{-15} erg cm^{-2} s^{-1} in band *B*.

J Flux in 10^{-15} erg cm^{-2} s^{-1} in band *CD*.

K Band in which S/N ratio is the highest

L Gap flag: can assume a value of 0 (good), 1 (fair), or 2 (poor) related to the fact that the X-ray source falls on inter-CCD gaps in one or more of the EPIC cameras, or close to the edge or outside the FOV of one EPIC camera and is based on the ratio of the punctual exposures in each camera to the maximum exposure in the FOV also for each camera. It can also assume the value -1 if the X-ray source is outside the FOV of at least one camera (there are no such cases in the 4σ sample).

M Identification rank: gives the quality of the identification with the counterpart, coded as 0 optimal e.g. only one counterpart, or brightest and closest; 1 good; 2 (dubious or ambiguous, e.g. typically more than one possible counterpart listed); 4 unidentified source.

N Distance in arcsec between X-ray source and counterpart in the following order of preference: the VVDS optical counterpart if any; or the radio counterpart in the VIRMOS 1.4 GHz catalogue (Bondi et al. 2003); or the radio counterpart in the XMM-LSS 325 MHz catalogue (Cohen et al. 2003); or the catalogued NED object; or the catalogued SIMBAD object. It is blank if there are no counterparts.

O *R* magnitude of counterpart from the VVDS catalogue. *R* and *I* magnitudes are non-blank when there is a valid measurement in the VVDS catalogue. They may be left blank also in case of radio counterparts only, or of (usually very bright) objects present *only* in external (SIMBAD) catalogues.

P Error on *R* magnitude.

Q *I* magnitude of counterpart.

R Error on *I* magnitude.

S Photometry reliability flag (derived from McCracken et al. 2003): 0 good; 1 flagged as possibly bad, but not saturated; 2 flagged as bad because saturated.

T A V indicates presence of a radio counterpart in VIRMOS 1.4 GHz catalogue (Bondi et al. 2003).

U An L indicates presence of a radio counterpart in the XMM-LSS 325 MHz catalogue (Cohen et al. 2003).

V Name of counterpart, precedence order is NED name, then SIMBAD name including VIRMOS 1.4 GHz catalogue then name in the radio catalogue by Cohen et al. (2003).

W Repetition of identifier in Col. A.

candidates within the given radius according to the formula by Downes et al. (1986) used e.g. by Brusa et al. (2003) or Mignoli et al. (2004)

$$p = 1 - \exp(-\pi\, n(<m)\, r^2)$$

where r is the distance between the X-ray source and the concerned optical candidate, and the density $n(<m)$ of optical objects having I magnitude brighter than the magnitude m of the candidate counterpart was computed using the full VVDS catalogue (McCracken et al. 2003). A $p < 0.01$ criterion (similar to the one used by Brusa et al. (2003) and more conservative than the one used by Mignoli et al. (2004), corresponding in our case e.g. to the probability of finding an $I = 21$ object at 2″) applied to the X-ray/optical pairs produces a list of identifications very similar to our visually identified sources. Namely 93% of our best identifications (rank 0) and 84% of the rank 1 associations have $p < 0.01$ (and only one of the rank 0 identification has $p \geq 0.02$), while only 21% of the ambiguous (rank 2) cases have $p < 0.01$.

At the present time, spectroscopy is in progress within the framework of different programs, and only a few of our identifications are spectroscopically confirmed.

6.2. Optical vs. X-ray properties

Figure 9 shows the angular separation between the position of the best optical counterpart identified according to the positional and photometric criteria (as described in Sect. 6.1) and the position of the X-ray source (after astrometric correction).

One can note the absence of systematic shifts. We also verified that there is no correlation between the X-ray to optical distance and the off-axis position in the field of view, while there is a mild correlation with count rate, in the sense that sources with a large X-ray to optical separation are among the weakest. We note moreover that 93% of the optical counterparts are within a 2″ radius from the X-ray source (99% within 4″). We therefore conclude that, after astrometric corrections have been applied, the search radius for optical counterparts can be safely reduced to 4″.

Figure 10 compares the distribution of optical magnitudes for the identified sources and for the ambiguous identifications, i.e. X-ray sources for which there are 2 or more candidate identifications in the search radius. As expected, unidentified sources populate the region of fainter magnitudes where the density of possible optical counterparts makes chance coincidences more probable. Spectroscopy or at least multicolor photometry is needed to increase the number of identifications and to determine the redshifts and types of the candidate counterparts. Work on the optical and multifrequency information already acquired within the VIMOS and XMM-LSS consortia is in progress.

We compute the X-ray to optical flux ratio using our R magnitudes (in the AB system) according to the formula

$$\log(F_X/F_R) = \log F_X + 5.51 + R_{AB}/2.5$$

where the constant derives from the standard conversion of AB magnitudes into monochromatic flux and from the integration of the monochromatic flux over the filter bandwidth assuming a flat spectrum.

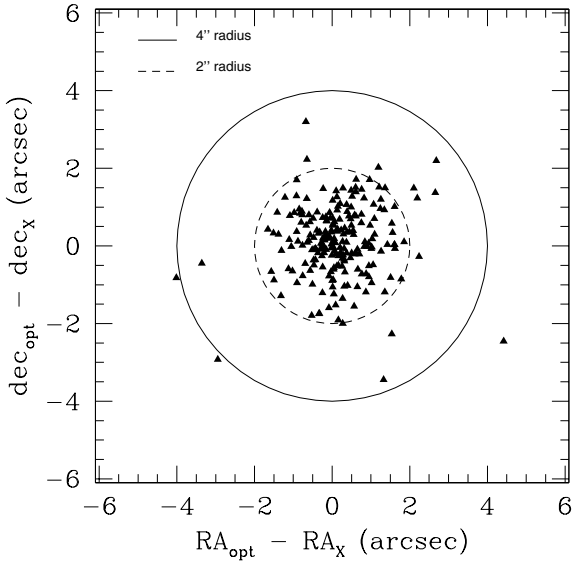

Fig. 9. Distance in RA and Dec between the X-ray source position (inclusive of astrometric correction) and the optical counterpart for well identified sources (ranks 0 and 1 in the database). Two fiducial radii of 2″ and 4″ are shown.

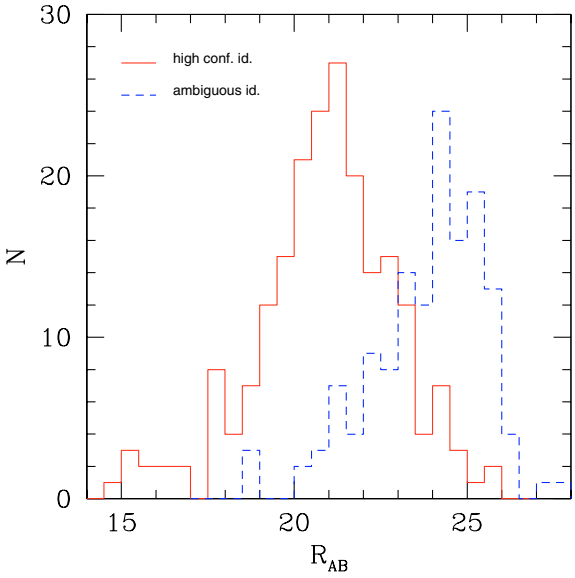

Fig. 10. R magnitude distribution for well identified sources (ranks 0 and 1 in the database, solid histogram) and for optical objects within 6″ from the ambiguously identified sources (rank 2, dashed histogram).

The X-ray to optical ratio for our identified sources is shown in Fig. 11 as a function of the X-ray flux (2−10 keV band). We have also included the ambiguous identifications (marked with different symbols) assuming that the brighter object is the true counterpart. The latter values should therefore be considered as lower limits for the X-ray to optical flux ratio: a few objects that are now in the "normal AGN" region could migrate upwards and populate the obscured AGN region.

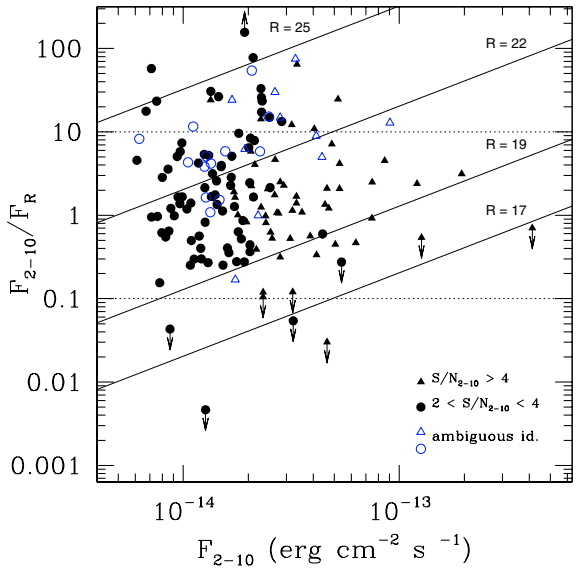

Fig. 11. X-ray to optical flux ratio (band *CD* vs. *R* magnitude) as a function of the X-ray flux (in band *CD*). The sources shown are those in the 4σ VVDS sample, detected above 2σ in band *CD*. Upper limits (on the X-ray to optical ratio) correspond to sources photometrically saturated (optical magnitude likely underestimated). Lower limits corresponds to sources without optical counterpart (1 association with a radio source only). Open symbols correspond to rank 2 sources (ambiguous identification, more than a counterpart, of which the brightest is used to derive the optical flux). Diagonal lines indicate loci of constant *R* magnitude while horizontal dotted lines mark the region of canonical AGNs ($0.1 < F_X/F_R < 10$).

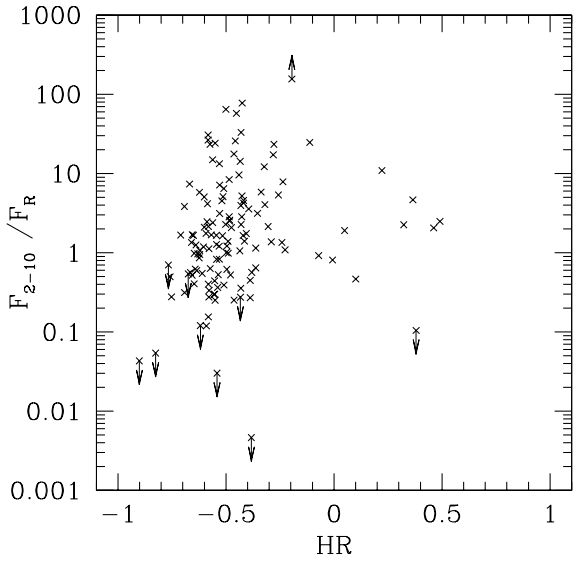

Fig. 12. X-ray (2−10 keV) to optical flux ratio vs hardness ratio for sources of the 4σ VVDS sample. Only sources with a significance of at least 2σ in one band (and of course 4σ in the other) are shown, provided they have a rank 0−1 identification (one case has only a radio counterpart). Upper limits are due to "saturated" optical counterparts which only yield a lower limit to the optical flux.

As expected, most (∼80%) of the sources lie in the region of classical AGNs ($0.1 < F_X/F_R < 10$), ∼3% are in the starburst – normal galaxy range ($F_X/F_R < 0.1$) and ∼17% (including optically blank fields) in the region expected for optically obscured AGNs ($F_X/F_R > 10$).

The percentage of high X-ray to optical ratio sources is only slightly lower than in other X-ray surveys of similar depth (e.g. 20% in Fiore et al. 2003). However, since the 4σ VVDS sample is not fully identified and since our identification procedure favours optically brighter objects, the real fraction of sources with $F_X/F_R > 10$ could be higher.

Figure 12 shows the X-ray to optical ratio vs the hardness ratio. As shown recently by Della Ceca et al. (2004) this diagram is a useful tool to separate stars from the extragalactic population, and to locate different kinds of AGN. Since we have used the X-ray flux in the 2−10 keV band (for comparison with Fig. 11), stars are not included in our diagram as they are not detected in the 2−10 keV band. We verified however that our confirmed stars (via SIMBAD or via preliminary results of VIMOS spectroscopy) fall in the expected location in the $F_{0.5-4.5}/F_R$ vs. HR_{cb} plot. Most of our sources populate the expected locus of AGNs, with a number of objects with very high (10–100) X-ray to optical ratios (suggesting optical extinction) and a few with hard X-ray spectra, pointing to X-ray absorbed nuclei. In a forthcoming paper we will take advantage of the full multifrequency and spectroscopic information to discuss the properties of the populations selected by the X-ray survey with respect to those of the optical survey.

Acknowledgements. This work is based on observations obtained with *XMM-Newton*, an ESA science mission with instruments and contributions directly funded by ESA Member States and the USA (NASA). This work has benefitted from many useful discussions with S. Andreon, A. Wolter and R. Della Ceca at INAF-OABrera.
OG, EG and JS would like to acknowledge support by contract Inter-University Attraction Pole P5/36 (Belgium) and by PRODEX (XMM-LSS)

References

Arnouts, S., Schiminovich, D., Ilbert, O., et al. 2005, ApJ, 619, L43
Baldi, A., Molendi, S., Comastri, A., et al. 2002, ApJ, 564, 190
Bondi, M., Ciliegi, P., Zamorani, G., et al. 2003, A&A, 403, 857
Brusa, M., Comastri, A., Mignoli, M., et al. 2003, A&A, 409, 65
Cohen, A. S., Röttgering, H. J. A., Kassim, N. E., et al. 2003, ApJ, 591, 640
Crawford, D. F., Jauncey, D. L., & Murdoch, H. S. 1970, ApJ, 162, 405
Della Ceca, R., Maccacaro, T., Caccianiga, A., et al. 2004, A&A, 428, 383
Dickey, J. M., & Lockman, F. J. 1990, ARA&A, 28, 215
Downes, A. J. B., Peacock, J. A., Savage, A., & Carrie, D. R. 1986, MNRAS, 218, 31
Fiore, F., Brusa, M., Cocchia, F., et al. 2003, A&A, 409, 79
Gehrels, N. 1986, ApJ, 303, 336
Harrison, F. A., Eckart, M. E., Mao, P. H., Helfand, D. J., & Stern, D. 2003, ApJ, 596, 944
Jansen, F., Lumb, D., Altieri, B., et al. 2001, A&A, 365, L1

Le Fèvre, O., Mellier, Y., McCracken, H. J., et al. 2004, A&A, 417, 839
Le Fèvre, O., Mellier, Y., McCracken, H. J., et al. 2005, A&A, in press [arXiv:astro-ph/0409133]
Lonsdale, C. J., Smith, H. E., Rowan-Robinson, M., et al. 2003, PASP, 115, 897
Maraschi, L., et al. 2003, Conference on Multiwavelength AGN Surveys, Dec 2003, Cozumel
McCracken, H. J., Radovich, M., Bertin, E., et al. 2003, A&A, 410, 17
Mignoli, M., Pozzetti, L., Comastri, A., et al. 2004, A&A, 418, 827
Moretti, A., Campana, S., Lazzati, D., & Tagliaferri, G. 2003, ApJ, 588, 696
Murdoch, H. S., Crawford, D. F., & Jauncey, D. L. 1973, ApJ, 183, 1
Pacaud, F., et al. 2005, in preparation
Pierre, M., Valtchanov, I., Altieri, B., et al. 2004, J. Cosmology Astropart. Phys., 09, 011
Radovich, M., Arnaboldi, M., Ripepi, V., et al. 2004, A&A, 417, 51
Strüder, L., Briel, U., Dennerl, K., et al. 2001, A&A, 365, L18
Tajer, M., Chiappetti, L., Trinchieri, et al. 2004, 6th National Conference on AGNs, May 2004, Volterra, http://www.arcetri.astro.it/~agn6/proceedings/
Turner, M. J. L., Abbey, A., Arnaud, M., et al. 2001, A&A, 365, L27
Waskett, T. J., Eales, S. A., Gear, W. K., et al. 2004, MNRAS, 350, 785
Yang, Y., Mushotzky, R. F., Steffen, A. T., et al. 2004, AJ, 128, 1501

Online Material

Appendix A: Comments on individual sources

- XMDS J022315.4–042558: it is identified with a bright spiral, present also in the NED database (b_J = 19.75), which however falls in a bad photometric area (close to VVDS border) and has no valid optical magnitudes.
- XMDS J022316.3–042007: it has as counterpart the bright (V = 11.0) star BD–04 388 which also falls in a bad photometric area close to VVDS border, and has no valid optical magnitudes; even if it didn't, it would have been saturated. The distance reported in the catalogue is overestimated, since the bright source in the VVDS catalogue is split in two by a saturated spike.
- XMDS J022330.9–044235: it is considered a dubious (rank 2) identification, since the closest object reported as rank 2 is faint (I = 24.5) and at 5.4″. It is a borderline case, which could perhaps be a blank field.
- XMDS J022337.3–040938: it coincides with a bright saturated (I < 14.6) starlike object, which matches a 7.9 mJy 325 MHz radio source, which is a lobe component of the multiple source CRK2003 J0223.6–0409. Another component is instead close to the NED object NVSS J022336−040932. Could it be that the star is a foreground object with respect to the radio source? The X-ray optical distance reported in the catalogue is overestimated, since the bright source in the VVDS catalogue is split in two by a saturated spike.
- XMDS J022403.7–043303: it has as counterpart the 16th magnitude object Markarian 1036, which is unfortunately saturated in the VVDS.
- XMDS J022403.9–041326: it falls inside a group of weak uncatalogued objects, which are affected by the spike of a bright star situated north of them. A radio object detected both in the VIRMOS 1.4 GHz catalogue and in our own observations at 325 MHz (CRK2003 J0224.0–0413) is at 13.6″ south. This source has a duplicate detection in a different pointing at 11.7″, and both are inside an unpublished galaxy cluster (Andreon, private communication).
- XMDS J022413.2–045723: it falls at a blank position in a small group of objects, unconfirmed yet as a spectroscopic group, of which the closest is at 2.6″. Note that this source is in field G18, which is not yet astrometrically corrected.
- XMDS J022445.4–043656: it is considered unidentified (rank 4), falling in a blank field since the closest object (rejected) is faint (I = 25.7) and at 5.0″.
- XMDS J022450.9–042903: its brightest and closest counterpart is a 21 mag object at 0.5″, however at 2.8″ there is a radio source detected in the VIRMOS 1.4 GHz survey as well as in our own 325 MHz data (CRK2003 J0224.8−0429). We kept it as a rank 2 source.
- XMDS J022454.7–040628: its brightest and closest counterpart is a 21 mag object at 1.1″, however there is a fainter object at 2″ which has also 1.4 GHz radio emission.
- XMDS J022456.0–041725: it appears to match positionally an uncatalogued enhancement in the periphery of the NED spiral galaxy 2MASX J02245534–0417351 (distance of the nucleus from the X-ray source 14.8″).
- XMDS J022524.8–044042: it is associated with a saturated bright elliptical, also listed in NED (b_J = 20.04) and as a VIRMOS 1.4 GHz radio source.
- XMDS J022530.6–041418 is one of the sources mentioned in Sect. 5 for which the observations in two different pointings give a marginal flux difference (3.5σ). Its counterpart is a saturated object (nominal VVDS I = 16.21), corresponding to the NED elliptical galaxy 2MASX J02253077−0414183.
- XMDS J022544.6–041936 is the other source in the VVDS/4σ catalogue mentioned in Sect. 5 for which the observations in two different pointings give a marginal flux difference (3.9σ). Its counterpart is also a saturated object (nominal VVDS I = 17.49), corresponding to the NED elliptical galaxy APMUKS(BJ) B022313.84–043304.3.
- XMDS J022606.6–040259: it is assigned rank 2 because the likely counterpart is not too close to the X-ray position and appears to be an unresolved double object.
- XMDS J022606.9–043316: its counterpart should be a background object masked behind the bright (V = 10.37) star BD–05 456 (which is too far to be the counterpart). For this reason, the line-of-sight association is classified as rank 2.
- XMDS J022713.6–043910: it has as counterpart the bright (V = 10.12) star BD–05 461 not included in the VVDS catalogue; if it were, it would have been saturated.
- XMDS J022714.2–042645: the finding chart is saturated by a bright star, BD–05 480, located southwards with respect to our target, whose position is partially behind a spike from the star. For this reason there are no objects listed in the VVDS catalogue, although an object is clearly visible behind the spike at approximately RA = 02:27:14.16 Dec = −4:26:45.0.
- XMDS J022721.7–044153: it has no nearby optical counterparts, but a very good positional coincidence (0.8″) with a VIRMOS 1.4 GHz radio source. Note that a 17 mag saturated object is however present 6″ north.
- XMDS J022725.1–043656: it is considered unidentified (rank 4), falling in a blank field since the closest object (rejected) is faint (I = 25.8) and at 4.2″.
- XMDS J022735.6–041317: it corresponds to a plethora of very faint objects all located inside an extended radio halo, whose central position matches very well the X-ray position.
- XMDS J022735.7–041122: there are two possible optical counterparts which are both located at the periphery, but inside the nominal extent, of the extended 325 MHz radio source CRK2003 J0227.6–0411 centered 19″ to the northeast. A 1.4 GHz point-like source, which is a component of a terribly elongated multiple object, is instead located in the X-ray error radius between the two optical objects, while the NED object NVSS J022736–041117 is located at 9″ midway between the X-ray source and the 325 MHz radio source.
- XMDS J022742.1–043607: there are no optical catalogued sources; an unresolved double source is present at 4″ just outside of the nominal error radius of the X-ray source and

within 1.1″ there is a 1.4 GHz radio point source. The finding chart is affected by the spikes of a nearby bright star.
- XMDS J022748.2–041013: it has no optical counterpart at all, hence is flagged as rank 4, blank field.
- XMDS J022812.5–045717: it is in field G15 which has not yet been astrometrically corrected.

Concerning spectral peculiarities, we can use as an indicator the fact that the energy band with the best signal to noise (Col. K of the catalogue) is not band *B*. We have only one source (XMDS J022410.7–042759) which is very soft (detected only in band *A*), and 10 cases with the best signal to noise in band CD (of these 7 are among the 16 not detected in the softer bands mentioned in Sect. 5.1).